Biosensors and Bioelectronics 312 (2026) 119064

Contents lists available at ScienceDirect

Biosensors and Bioelectronics

journal homepage: www.elsevier.com/locate/bios

Development of itch biosensors with engineering membrane receptors that are coupled to field-effect transistors

Lulu Guo [a,b,*,1], Weifeng Zhang [b,c,1], Xuan Li [d,1], Canyang Niu [c,e,1], Zili Liu [f,1], Zaiyu Zhang [g,1], Honghao Fan [d], Xihe Gao [c], Kaiyu Wang [b,c], Haoran Liu [d], Chunhong Zhang [a], Ying Li [j,**], Ziran Wang [g,***], Fan Yang [d,****], Guoqiang Li [h,*****], Jinpeng Sun [b,c,f,i,******]

[a] Department of Dermato-Venereology, The Second Hospital, Cheeloo College of Medicine, Shandong University, Jinan, China
[b] Advanced Medical Research Institute, Cheeloo College of Medicine, Shandong University, Jinan, Shandong, 250012, China
[c] New Cornerstone Science Laboratory, Department of Biochemistry and Molecular Biology, School of Basic Medical Sciences, Cheeloo College of Medine, Shandong University, Jinan, Shandong, 250012, China
[d] Key Laboratory Experimental Teratology of the Ministry of Education and Department of Physiology, School of Basic Medical Sciences, Shandong University, Jinan, Shandong, 250012, China
[e] Research Center for Cardiopulmonary Rehabilitation, University of Health and Rehabilitation Sciences Qingdao Hospital (Qingdao Municipal Hospital), School of Health and Life Sciences, University of Health and Rehabilitation Sciences, Qingdao, China
[f] Department of Physiology and Pathophysiology, School of Basic Medical Sciences, State Key Laboratory of Vascular Homeostasis and Remodeling, Beijing Key Laboratory of Cardiovascular Receptors Research, Peking University, Beijing, 100191, China
[g] School of Mechanical Engineering, Key Laboratory of High Efficiency and Clean Mechanical Manufacture, Ministry of Education, Shandong University, Jinan, 250000, China
[h] School of Flexible Electronics & State Key Laboratory of Optoelectronic Materials and Technologies, Sun Yat-sen University Shenzhen, Guangdong, 510275, China
[i] NHC Key Laboratory of Otorhinolaryngology, Qilu Hospital of Shandong University, Jinan, Shandong, 250012, China
[j] Department of Dermatology, Qilu Hospital of Shandong University, Jinan, Shandong, 250012, China

ARTICLE INFO

Keywords:
Itch bioelectronic sensor
Mas-related G-protein coupled receptor member X2 (MRGPRX2)
Graphene field-effect transistors (GFET)
Atopic dermatitis (AD)
Clinical diagnostics

ABSTRACT

Biosensors inspired by biological sensory systems are valuable tools for detecting physiological and environmental stimuli with high degrees of specificity and sensitivity. An itch irritant biosensor to detect environmental changes or pruritogenic substances in human blood or tissues highly associated with inflammation and prevalent conditions like atopic dermatitis (AD) has not been developed. To address this gap, we developed a novel bioelectronic sensor by integrating the human itch receptor Mas-related G-protein-coupled receptor X2 (MRGPRX2) with a graphene field-effect transistor (GFET). This MRGPRX2–GFET biosensor covalently immobilizes functional receptors, enabling direct conversion of ligand-binding events into quantifiable electrical signals. We demonstrate that the sensor can detect known MRGPRX2 agonists with exceptional sensitivity and specificity, achieving a detection limit for SP at approximately 7 pM. Molecular dynamics (MD) simulations and mutational effects reveal that ligand binding induces cytoplasmic conformational rearrangements in MRGPRX2, strengthening receptor–graphene coupling and providing a mechanistic basis for signal transduction. Importantly, the biosensor effectively distinguishes plasma samples from AD patients and healthy controls by capturing different electrical signal responses. In our study, we establish a versatile platform for diagnosing and subtyping chronic

* Corresponding author. Department of Dermato-Venereology, The Second Hospital, Cheeloo College of Medicine, Shandong University, Jinan, China.
** Corresponding author.
*** Corresponding author.
**** Corresponding author.
***** Corresponding author.
****** Corresponding author. Advanced Medical Research Institute, Cheeloo College of Medicine, Shandong University, Jinan, Shandong, 250012, China.
E-mail addresses: lulu_guo@sdu.edu.cn (L. Guo), dr.liying@email.sdu.edu.cn (Y. Li), wangziran@sdu.edu.cn (Z. Wang), yangfan1357@163.com (F. Yang), liguoqiang@mail.sysu.edu.cn (G. Li), sunjinpengsdu@126.com (J. Sun).
[1] These authors contributed equally to this work.

https://doi.org/10.1016/j.bios.2026.119064
Received 18 May 2026; Received in revised form 14 July 2026; Accepted 22 July 2026
Available online 23 July 2026

itch disorders and offer a generalizable strategy for developing membrane receptor-based multiplexed "itch-print" biosensors.

1. Introduction

Biosensors inspired by biological sensory systems, such as olfaction, taste, vision, and nociception, have the potential to serve as valuable equipment for detecting physiological and environmental stimuli with high degrees of specificity and sensitivity (Son et al., 2017; Son and Park, 2018; Su et al., 2023; Yang et al., 2021b). In general, a biosensor consists of a biosensing element and a signal conversion element. On the basis of the type of biosensing element, biosensors can be categorized into sensors that detect enzymes, antibodies, nucleic acids, cells, aptamers, peptides and receptors (Flynn et al., 2023; Kumari and Suryabai, 2024). Among these types, sensors based on naturally evolved membrane receptors provide minimal interference, exceptional selectivity, and high sensitivity (Gin et al., 2024; Qing et al., 2023). Several examples utilize G protein-coupled receptors (GPCRs) as molecular recognition elements to detect light or odour (Seo et al., 2025). Recently, a TAAR13c/d-based biosensor has been generated to detect food spoilage and fruit ripeness; another example is GPCR-activation-based (GRAB) sensors that utilize D1R and 5-HTR4, enabling multiplexed, high-resolution imaging of dopamine and serotonin dynamics in vivo (Deng et al., 2024; Kim et al., 2022; Zheng et al., 2024).

In addition to light and odour, many important sensory experiences, such as itch (pruritus), are mediated by GPCRs, providing opportunities for the use of GPCRs to design itch biosensors (Bader et al., 2014; Meixiong and Dong, 2017). Itch plays an essential protective role, alerting the body to potential hazards such as parasites or irritating substances to avoid environmental harm (Baral et al., 2016; Liu et al., 2025). When an itching sensation becomes chronic, it is considered a debilitating symptom of various dermatologic or systemic conditions, including atopic dermatitis (AD) and allergic contact dermatitis (ACD) (Guttman-Yassky et al., 2025; Meixiong et al., 2019). AD is frequently associated with a spectrum of comorbid conditions, including allergic rhinitis, asthma, and conjunctivitis. The persistent and refractory nature of these conditions can lead to psychological complications, such as depression, thereby imposing a substantial burden on both individual quality of life and the broader socioeconomic health care system (Prevalence and attributable, 2020;Guttman-Yassky et al., 2025). Importantly, these disorders are mediated by the release of multiple pruritogenic substances, such as substance P (SP), which activate specific human itch receptors, such as MRGPRX2 (Kühn et al., 2021). The design and development of itch biosensors can help people monitor hazards in the environment and provide useful tools for clinical diagnostics.

Current methodologies for the detection of itch irritants and clinical AD/ACD biomarkers primarily include enzyme-linked immunosorbent assays (ELISAs), radio immunoassays (RIAs), and liquid chromatography coupled with tandem mass spectrometry (LC–MS/MS) (Beaudry and Vachon, 2006; Li et al., 2020; Michaels et al., 1998; Nyberg et al., 1985). ELISAs offer relatively high throughput and cost effectiveness but can suffer from limitations in sensitivity, specificity, and susceptibility to matrix effects, potentially leading to false positives or negatives (de Araujo et al., 2024; Kharlamova et al., 2021). RIAs can be highly sensitive, but they involve the use of radioactive isotopes, posing safety and disposal concerns (Rezaei et al., 2009). While LC–MS/MS is considered the gold standard because of its high specificity and quantification accuracy, it requires sophisticated instrumentation, extensive sample preparation, and skilled personnel, and it is often time-consuming and expensive, rendering it less suitable for rapid or point-of-care diagnostics (Jogiraju et al., 2025; Zhang et al., 2025a). Consequently, a rapid, sensitive, and convenient itch biosensor is urgently needed to quantify pathophysiological itch irritants in environmental and clinical samples.

GFET biosensors have emerged as a promising approach for label-free, real-time biomolecular sensing and are ideal for detecting low-abundance analytes in complex media because of their exceptional sensitivity (Bodily et al., 2023; Seo et al., 2025). While GFETs functionalized with odorant GPCRs have demonstrated promise for volatile compound sensing (Kim et al., 2022), translating this biosensing platform into clinical diagnostics for conditions such as AD faces three fundamental barriers spanning clinical practice and technological design. Clinically, routine AD diagnosis relies on subjective phenotypic scoring, which yields inconsistent assessments for atypical cases, whereas previous serological markers such as total IgE fail to capture the full pruritogenic bioactivity driving itch pathology. Technologically, existing FET platforms exhibit other two critical limitations: they quantify only discrete surrogate markers (skin pH, sweat electrolytes, IgE, inflammatory cytokines) rather than AD-specific itch-inducing bioactivity, and the signal transduction mechanism linking activated GPCRs to graphene surfaces remains unresolved, precluding rational optimization of receptor–electrode interfaces (Laliberte et al., 2022; Ohno et al., 2010; Park et al., 2021; Ren et al., 2023; Wang et al., 2020). To overcome these challenges, we developed an itch-GPCR-based functional biosensing strategy that harnesses the human itch receptor MRGPRX2 as a dynamic and conformational selective recognition element, integrates mechanistic MD simulations with receptor engineering, and validates the platform in clinical AD plasma samples.

Previous studies, including our own, have identified at least 13 GPCRs associated with itch signaling (Afrooghe et al., 2025; Al Hamwi et al., 2022; Alemi et al., 2013; Deng et al., 2023; Emrick et al., 2018; Guo et al., 2023; Jin et al., 2025; Lieu et al., 2014; Liu et al. 2011, 2022, 2023; Ohsawa and Hirasawa, 2012; Yang et al. 2021a, 2024). In parallel with the current work, we reported that more than 80% of clinical AD patients have increased activity of the itch receptor MRGPRX2 and identified clinically relevant itch irritants. Notably, a de novo protocol to measure GPCR activity induced by clinical samples was designed, and blocking MRGPRX2 activity showed therapeutic potential for treating AD. However, the method used in that manuscript is labour intensive and requires relatively large quantities of clinical samples. In parallel with that work, we developed a novel biosensor based on human MRGPRX2 to provide highly convenient and efficient screening equipment. By covalently immobilizing functional MRGPRX2 on a GFET platform, we constructed a device that directly converts receptor–ligand interactions into quantifiable electrical signals. We showed that this MRGPRX2–GFET biosensor could detect known agonists such as SP with high sensitivity and specificity. Utilizing previously established fabrication protocols of GFET device architecture, we developed a functional bioelectronic transduction paradigm and provide mechanistic insight into GPCR-to-FET signal conversion. Unlike previous GFET biosensors that rely on static affinity probes (e.g., antibodies or aptamers) for molecular quantitation, our sensor harnesses MRGPRX2 as a dynamic, conformation-responsive recognition element. This allows the device to report integrated pruritogenic bioactivity rather than merely reflecting the abundance of a single analyte. We further combined all-atom molecular dynamics (MD) simulations with cytoplasmic hydrophobic mutation ($MRGPRX2^{6F}$) to elucidate the mechanism and boost electrical signals without impairing ligand binding. Moreover, our itch-receptor based biosensor successfully differentiated plasma samples from AD patients and healthy controls by capturing a distinct "itch fingerprint" that was indicative of MRGPRX2 overactivation. Given the diversity of itch receptors, including MRGPRX1, MRGPRX4 and histamine receptors, this platform could be readily expanded into a multiplexed "itch-print"

sensor array, offering a potential tool for diagnosing, subtyping, and monitoring chronic itch disorders.

2. Results

2.1. Bioinspired strategy for itch-irritant detection

To enable the rapid and objective diagnosis of AD, a chronic condition often triggered by environmental fluctuations and irritants, we developed a bioelectronic sensor that emulated the molecular mechanism of human itch perception (Fig. 1 and Fig. S1). This bioelectronic sensor specifically targeted pruritogenic biomarkers, such as substance P (SP) and PAMP9-20, whose expression levels were upregulated by environmental triggers. Leveraging the precise signal transduction capabilities of biological sensory mechanisms, we utilized human MRGPRX2, a key mediator of nonhistaminergic itch, as the molecular recognition element. By covalently immobilizing purified MRGPRX2 onto a high-sensitivity GFET via a 1-pyrenebutanoic acid succinimidyl ester (PBASE) interfacial linker, the sensor directly translated specific ligand–receptor binding events into quantifiable electrical variations, which were manifested as Dirac point shifts. The resulting bioelectronic sensor achieved a detection limit in the picomolar range with a linear response to ligand concentration. Crucially, the high sensitivity performance allowed the sensor to effectively differentiate between plasma samples from AD patients and healthy controls by capturing a distinct electrical "itch fingerprint" that was indicative of MRGPRX2-receptor activation. This sensor provided a rapid and sensitive platform for the pathological diagnosis of AD, enabling the quantifiable detection of itch-related biomarkers in clinical blood samples.

2.2. Purified itch receptor biosensor coupled to PBASE

To develop a rationally designed activity-dependent ligand-selective itch sensor according to the use of GPCRs, we adopted a multistep GPCR modification strategy in which MRGPRX2 was used as a template (Fig. 2a). We employed an in vitro receptor purification system in Expi293 F cells. To increase the expression of MRGPRX2, we fused a BRIL tag at the N-terminus of full-length wild-type MRGPRX2. To avoid potential interference from the BRIL tag in subsequent experiments, we added a TEV proteolytic cleavage site adjacent to the BRIL tag. The purified fusion protein underwent TEV protease digestion to excise the BRIL tag, followed by size-exclusion chromatography (SEC) under native conditions. A major elution peak at ~15 mL, which corresponded to monomeric MRGPRX2, was detected for subsequent applications. SDS–PAGE analysis confirmed that the protein bands were correctly positioned at each purification stage (Fig. 2b). The size distribution and homogeneity of the MRGPRX2 protein ($MRGPRX2^{LMNG}$) embedded with LMNG were analysed by dynamic light scattering (DLS). The average diameters of LMNG and $MRGPRX2^{LMNG}$ were 6.5 nm and 11.7 nm, respectively (Fig. 2c). To couple MRGPRX2 to the graphene surface, we employed the crosslinker PBASE, which reacted with the amine groups on the protein and exhibited a characteristic fluorescence emission peak at approximately 376 nm (Bains et al., 2011). After incubation with PBASE or control solvent (DMF, N, N-Dimethylformamide), the MRGPRX2–PBASE conjugate resulted in a more pronounced fluorescent band at 36 kDa following PNGase treatment, indicating successful covalent linkage (Fig. 2d). We further assessed whether the functional activity of MRGPRX2 was preserved after PBASE modification using a FlAsH–BRET assay, which we established to monitor ligand-induced conformational changes in MRGPRX2 in our previous studies (Yang et al., 2021a) (Fig. 2e). The results showed that $MRGPRX2^{PBASE}$ still maintained functional activity and ligand selectivity, with only MRGPRX2-specific agonists eliciting FlAsH–BRET signal. In contrast, the BAM8-22, another itch receptor MRGPRX1 agonist, as well as the AT1R agonist angiotensin II, showed no detectable stimulatory effect (Fig. 2e–h and Fig. S2a–e). Considered together, these findings indicated that PBASE-modified MRGPRX2 maintained ligand recognition ability and could be utilized as a detector element for itch GPCR sensors.

2.3. Construction and interface characterization of the GFET-based itch receptor biosensor

To construct the MRGPRX2–GFET itch receptor biosensor, a field-effect transistor was fabricated on a SiO_2/Si substrate by patterning metal electrodes and transferring monolayer graphene (Fig. 3a and Fig. S1). The graphene surface was then functionalized with PBASE, followed by the covalent immobilization of the $MRGPRX2^{LMNG}$ receptor, resulting in the formation of a complete electrical itch sensor (Fig. 3b). In the microscopy image of the MRGPRX2–GFET region, the blue area corresponded to the graphene-covered surface (Fig. 3c). Raman

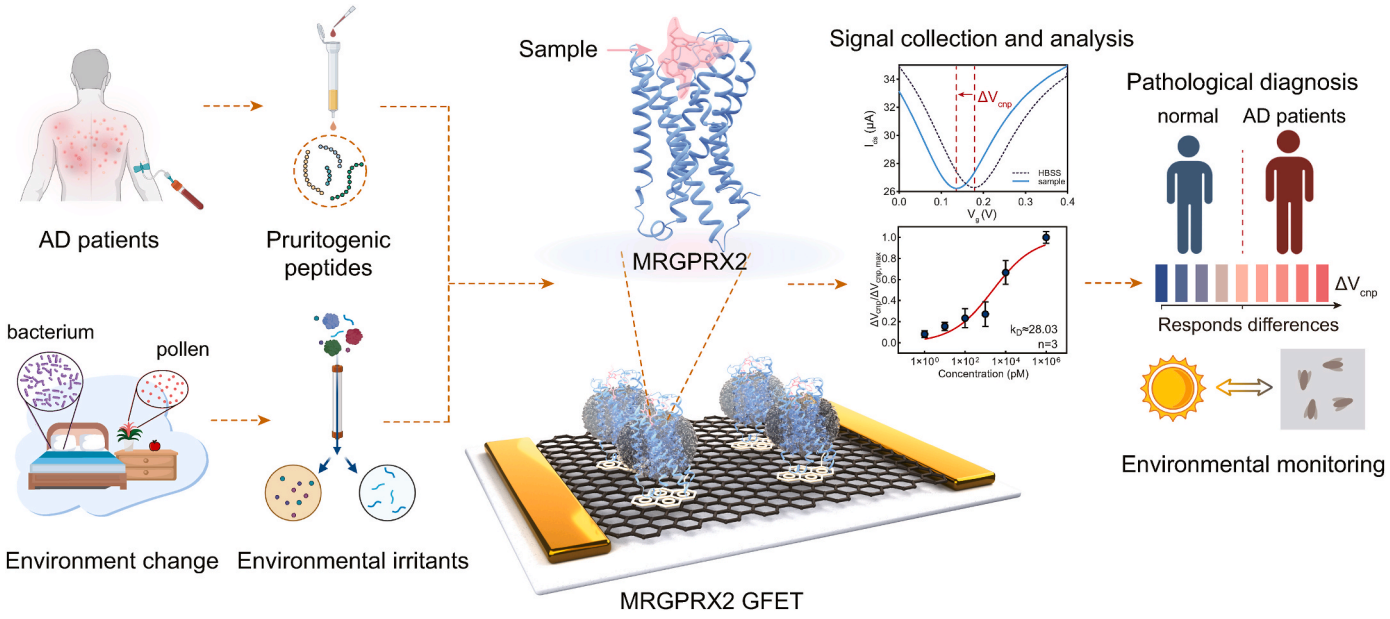

Fig. 1. Development of itch-receptor biosensor based on GFET
A schematic of the biosensor MRGPRX2 GFET testing process utilized throughout the paper.

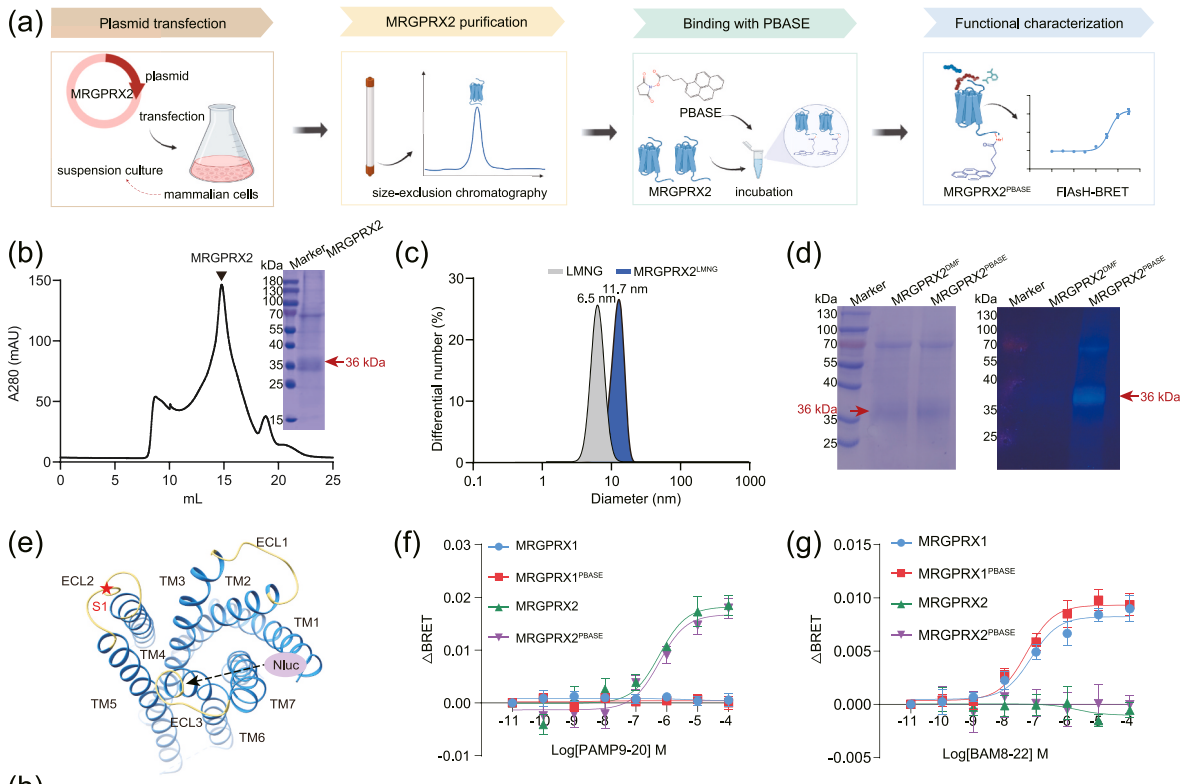

(h)

Ligand	Receptor	MRGPRX2		MRGPRX2^{PBASE}		MRGPRX1		MRGPRX1^{PBASE}	
		EC_{50} (nM)	Emax	EC_{50} (nM)	Emax	EC_{50} (nM)	Emax	EC_{50} (nM)	Emax
PAMP9-20	MRGPRX2	636.3 ± 32.2	0.018 ± 0.0002	586.9 ± 23.7	0.018 ± 0.0005	ND	ND	ND	ND
SP	MRGPRX2	822.4 ± 27.8	0.020 ± 0.0004	862.5 ± 22.0	0.020 ± 0.0003	ND	ND	ND	ND
C48/80	MRGPRX2	496.3 ± 11.9	0.019 ± 0.0003	494.0 ± 12.5	0.019 ± 0.0005	ND	ND	ND	ND
C14	MRGPRX2	575.1 ± 17.0	0.018 ± 0.0002	552.4 ± 17.9	0.017 ± 0.0001	ND	ND	ND	ND
GPR15L	MRGPRX1 & MRGPRX2	1606 ± 52.0	0.010 ± 0.0001	1433 ± 106.8	0.010 ± 0.0003	8638 ± 375.8	0.006 ± 0.0001	8526 ± 314.7	0.007 ± 0.0004
BAM8-22	MRGPRX1	ND	ND	ND	ND	76.3 ± 5.4	0.008 ± 0.0002	71.5 ± 11.0	0.009 ± 0.0004
AngII	AT1R	ND	ND	ND	ND	ND	ND	ND	ND

Fig. 2. Purification of itch-receptors MRGPRX2 produced in HEK293F cells and characterization of PBASE-coupled MRGPRX2.
(a) A schematic illustrating the overall flow of the purification of itch-receptors MRGPRX2 and the characterization assay following PBASE conjugation, cartoon elements were obtained from BioRender.
(b) Representative elution profiles of in vitro reconstituted MRGPRX2 on Superose 200 increase 10/300 column and SDS-PAGE results of the size-exclusion chromatography peak. MRGPRX2 band was shown by the red arrow at 36 kDa.
(c) DLS profiles for particle size distribution analysis of each ND.
(d) Direct visualization of protein-PBASE conjugation. SDS-PAGE analysis of the protein following incubation with PBASE. The resulting fluorescent bands upon UV illumination demonstrate successful covalent modification of the protein by PBASE. MRGPRX2 band was shown by the red arrow at 36 kDa.
(e) Schematic representation of the FlAsH-BRET assay. The Nluc was inserted at the N-terminal of wild-type MRGPRX2 and the FlAsH motifs were inserted at the second extracellular loop of MRGPRX2.
(f-g) Representative dose response curve of the different ligand (f: PAMP9-20, g: BAM8-22) induced BRET ratio in free or PBASE-covalently conjugated FlAsH-BRET sensor of MRGPRX1 or MRGPRX2. Data are presented as mean ± S.E.M.
(h) Tabulated EC50 and Emax values from dose-response fitting for all ligand–receptor combinations; ND indicates no detectable receptor activation. Ligand panel covers MRGPRX2-specific agonists (PAMP9-20, SP, C48/80, C14), MRGPRX1 agonist BAM8-22, dual-agonist GPR15L, and off-target AngII negative control. (For interpretation of the references to colour in this figure legend, the reader is referred to the Web version of this article.)

spectroscopy supported the successful transfer of monolayer graphene onto the silicon wafer, as indicated by characteristic Raman peaks at ~1585 cm^{-1} (G band) and ~2681 cm^{-1} (2D band), with the 2D peak intensity exceeding that of the G peak. The I_{2D}/I_G ratio of ~2.02 further indicates the monolayer nature of the transferred graphene. Upon PBASE modification, the Raman spectrum shows pronounced changes: the D band at ~1343 cm^{-1} intensifies significantly, indicating interfacial perturbation induced by PBASE–graphene interactions. Meanwhile, the I_{2D}/I_G ratio decreases from ~2.02 to ~1.22, reflecting alterations in the local electronic and vibrational environment of the graphene lattice (Fig. 3d). Field-emission scanning electron microscopy (FE-SEM) of the MRGPRX2 receptor-coupled sample revealed particulate structures averaging 11.7 nm in diameter (Fig. 2c), a size consistent with DLS data and confirmed by Negative Staining Transmission Electron Microscopy (NS-TEM) (Figs. 2c and 3e). These FE-SEM images demonstrated that the MRGPRX2 receptor protein was successfully coupled to the graphene through PBASE (Fig. 3e). Furthermore, energy dispersive spectroscopy (EDS) analysis of the receptor-coupled sample revealed the presence of C, N, and S (in addition to Si), which was in agreement with the elemental composition of the graphene and the MRGPRX2 protein, thereby confirming the successful conjugation of MRGPRX2 receptors onto the graphene surface (Fig. 3f). Additionally, AFM images were

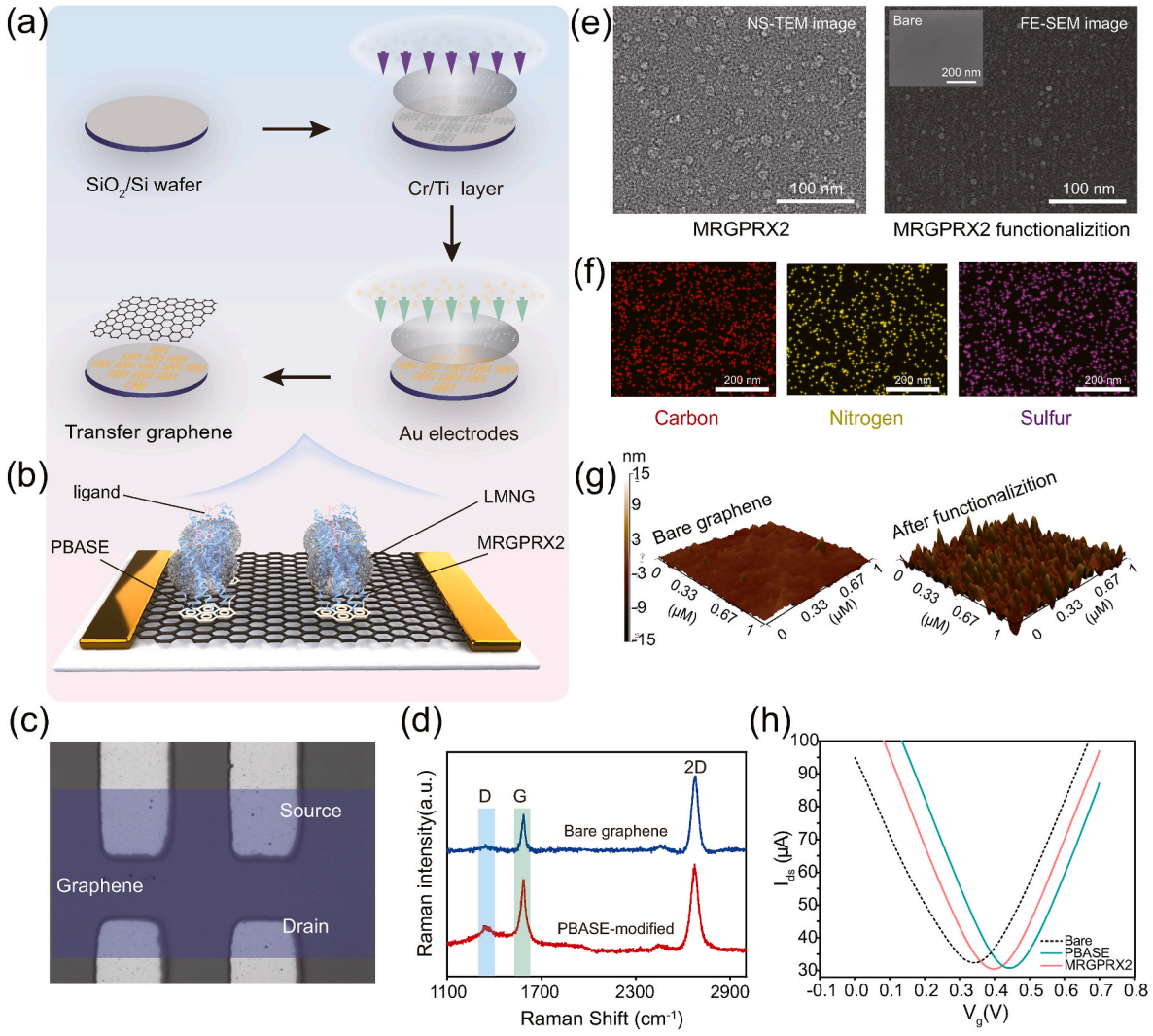

Fig. 3. Fabrication and biochemical functionalization of the biosensor
(a) Illustration of the fabrication and detection process of the GFET biosensor.
(b) Illustration of the GFET-Based itch-receptor biosensor.
(c) Optical micrographs of the source and drain electrodes as well as the channel of the GFET biosensor.
(d) Raman spectrum of graphene before and after surface modification of PBASE.
(e) NS-TEM (left) and FE-SEM (right) images of $MRGPRX2^{LMNG}$.
(f) EDS characterization on the graphene surface before and after receptor functionalization (scale bars: 200 nm).
(g) AFM images of the graphene surface before and after receptor immobilization.
(h) Transfer characteristic curves of the biosensor before and after PBASE and receptor modification.

obtained to visualize the nanoscale conjugation pattern of MRGPRX2 on the graphene, revealing distinct height profiles corresponding to protein adsorption (Fig. 3g). After the MRGPRX2 receptor protein was coupled, the electrical properties of the graphene were further analysed. The charge neutrality point voltage (V_{cnp}), the gate voltage (V_g) at which the drain-source current (I_{ds}) reached its minimum, decreased from 0.44 V to 0.40 V after MRGPRX2 was coupled to the graphene surface (Fig. 3h). These results illustrated the successful integration of the MRGPRX2–GFET itch receptor biosensor using the GFET and MRGPRX2 receptors, indicating the effective establishment of a stable bioelectronic interface that enabled efficient functional receptor immobilization. The observed shift in the Dirac point further indicated a change in the local charge distribution on the graphene surface upon receptor conjugation, confirming that the functionalized graphene could respond sensitively to biomolecular interactions. This integration provided a solid foundation for the subsequent detection of itch-related irritants, validating the feasibility of the MRGPRX2–GFET itch receptor biosensor as a robust platform for itch-related irritant bioelectronic sensing applications.

2.4. Electrical response and performance evaluation of the itch receptor GFET sensor

To evaluate the ability of the MRGPRX2-functionalized GFET sensor to sense pruritogenic biomarkers, we employed SP, a well-known MRGPRX2 agonist and an inflammatory neuropeptide that is critically implicated in AD and ACD, as a representative analyte (Bieber, 2022; Voisin and Chiu, 2019). We observed that the charge neutrality point voltage (V_{cnp}) of the MRGPRX2–GFET itch receptor biosensor shifted progressively from 0.35 V to 0.29 V in response to increasing concentrations of the SP ligand, which ranged from 1 pM to 1 μM, as indicated by the corresponding transfer curves (Fig. 4a and b). Importantly, this electrical response was absent in control GFET sensors lacking the MRGPRX2 receptor protein (Fig. 4a–e). Similarly, other MRGPRX2 ligands, such as PAMP9-20, induced specific electrical signalling

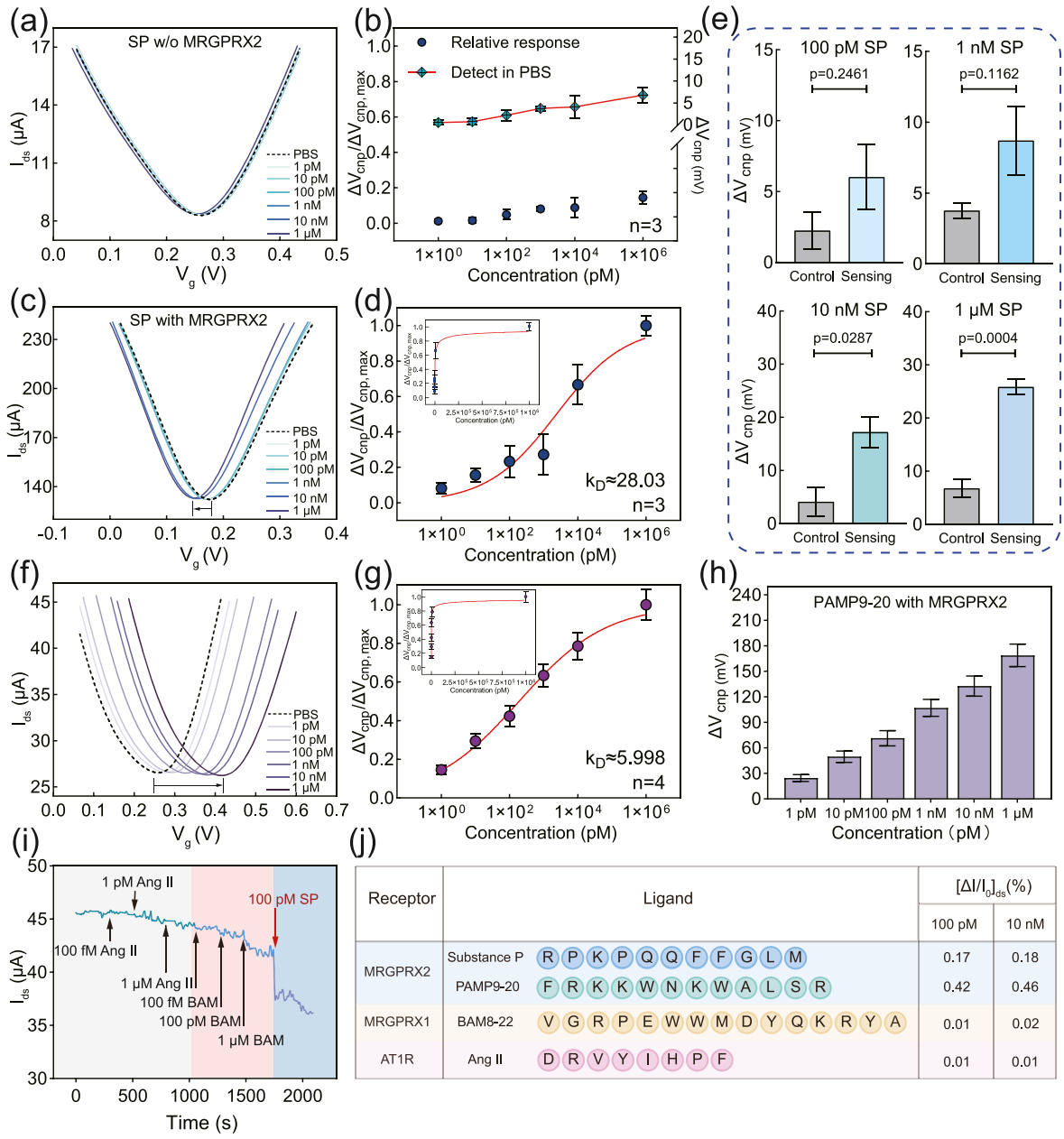

Fig. 4. Characterization and electrical measurements of GFET-Based itch-receptor biosensor.
(a) Transfer characteristic curves measured when GFET without itch-receptor biosensor was exposed to different SP-concentrations in PBS.
(b) Normalized Dirac point shift $\Delta V_{cnp}/\Delta V_{cnp,max}$ as a function of SP concentrations.
(c) Transfer characteristic curves measured when GFET-Based itch-receptor biosensor was exposed to different SP-concentrations in PBS.
(d) Normalized Dirac point shift $\Delta V_{cnp}/\Delta V_{cnp,max}$ as a function of SP concentrations.
(e) The shift of V_{cnp} of the GFET-Based itch-receptor and GFET without itch-receptor biosensor that interacted with increasing SP concentration in PBS (n = 3).
(f) Transfer characteristic curves measured when GFET-Based itch-receptor biosensor was exposed to different PAMP9-20-concentrations in PBS.
(g) Normalized Dirac point shift $\Delta V_{cnp}/\Delta V_{cnp,max}$ as a function of PAMP9-20 concentrations.
(h) The shift of V_{cnp} of the GFET-Based itch-receptor that interacted with increasing PAMP9-20 concentration in PBS (n = 4).
(i) A list of various specific ligands corresponding to different receptors. The table also shows the changes in current (ΔI_{ds}) versus time for various ligands.
(j) Primary chemical structures of the ligands corresponding to different receptors. Changes in current (ΔI_{ds}) versus time for various ligand.

responses (Fig. 4f–h and Fig. S4a). As the concentration of PAMP9-20 increased from 1 pM to 1 μM, the V_{cnp} of our sensor progressively shifted from 0.42 V to 0.22 V. These results collectively demonstrated that the presence of a functional MRGPRX2 receptor protein was indispensable for enabling the MRGPRX2-functionalized GFET sensor to selectively detect itch-related ligands. We next examined the ligand specificity of the MRGPRX2–GFET itch receptor sensor. G protein dissociation assays demonstrated that MRGPRX2 is selectively activated by its specific ligands with or without PBASE modification, and the downstream signaling potency (EC50) and efficacy (Emax) were similar (Fig. S3a–h). Similarly, the sensor responded robustly to its endogenous ligand, SP (100 pM), but exhibited no detectable response when exposed to relatively high concentrations (100 nM) of angiotensin II (AngII, the endogenous ligand for AT1R) or BAM8-22 (the endogenous ligand for MRGPRX1), indicating its specific response to only MRGPRX2-recognizing itch peptides (Fig. 4i–j and Fig. S4b–c). These

results demonstrated that the MRGPRX2–GFET itch receptor biosensor functioned as an activity-dependent receptor/ligand-selective itch biosensor.

2.5. Molecular mechanism underlying itch electrical signal transduction revealed by molecular dynamics simulations and mutational studies

To investigate the potential mechanism underlying the conversion of itch recognition to electrical signals via MRGPRX2-based itch biosensors, we constructed a tripartite molecular system comprising a MRGPRX2 receptor, a 1-pyrenebutyric acid N-hydroxy succinimide ester (PBASE) linker, and a graphene substrate. The pyrene moiety of PBASE was anchored onto the graphene surface via π–π stacking, while the NHS ester group covalently reacted with a lysine residue at the intracellular C-terminus of MRGPRX2 to form a stable amide bond (Fig. 5a and Fig. S5a). To assess the interaction between PBASE and the graphene substrate, the centre-of-mass (COM) distance between the pyrene group of PBASE and the graphene plane was monitored throughout the simulation. This distance remained consistently less than 6 Å, indicating stable π–π stacking interactions (Fig. 5b).

To further examine how ligand binding affected receptor–surface interactions, we introduced two representative peptide ligands—substance P (SP) and PAMP9-20—into the simulation system. Upon ligand binding with apo MRGPRX2, we observed a further reduction in the centre-of-mass (COM) distance between the PBASE moiety and the graphene surface, indicating that ligand binding could induce conformational rearrangements that brought the intracellular amino acids of the receptor closer to the graphene substrate (Fig. 5c–e). To quantitatively assess the strength of this interaction, we performed MM/GBSA calculations. The results showed that ligand binding led to a more favourable receptor–graphene binding free energy, particularly because of a significant increase in the van der Waals/hydrophobic interaction component. Our computational simulation suggested that ligand-induced conformational changes improved the degree of hydrophobic contact and surface complementarity between the receptor and the graphene interface (Fig. 5f).

Our simulation results indicated that 6 cytoplasmic side residues of MRGPRX2 (I135, R138, C139, S213, R214, and G215) frequently interacted with the graphene surface. Therefore, we hypothesized that the mutation of these residues into more hydrophobic residues, such as phenylalanine (F), could increase π−π stacking and improve itch electrical signal transduction responses (Fig. 5g). Compared with that of the wild type of MRGPRX2, the itch sensation of SP caused by the combined mutation of all 6 residues into F (I135F, R138F, C139F, S213F, R214F, G215F) in MRGPRX2 (MRGPRX2^{6F}) did not significantly change, as determined by a G protein dissociation assay (Lin et al., 2025; Yang et al., 2025) (Fig. 5h). Using the same purification approach, we prepared the MRGPRX2^{6F} protein and constructed a MRGPRX2^{6F}–GFET itch receptor biosensor. With increasing concentration of SP, the Dirac point shifted towards negative gate voltages; moreover, the response of MRGPRX2^{6F} was significantly greater than that of wild-type MRGPRX2 (Fig. 5i–j and Fig. S5b–d). Collectively, these results indicated that the itch irritant induced additional hydrophobic contact sites between the receptor cytoplasmic side, and the graphene surface played a determinant role in itch-electrical signal transduction, which could facilitate receptor-based biosensor design with improved responses.

2.6. Application of the itch receptor biosensor for analysing complex biological matrices (blood)

Previous studies have demonstrated that Mrgprb2 (the mouse orthologue of human MRGPRX2) plays an important role in the pathogenesis of AD (Roy et al., 2021). We therefore speculated that our MRGPRX2–GFET itch receptor biosensor could be applicable to human blood samples and be used to identify potential itch-related irritants and facilitate AD diagnosis. We then designed a cross-sectional study of 20 individuals who were diagnosed with AD; excluding those who were pregnant or immunodeficient; or those who were administered immunosuppressants 4 weeks before recruitment (Fig. 6a and Table S1). AD patients were diagnosed by two dermatologists according to the criteria of Hanifin and Rajka and the consensus criteria of the American Academy of Dermatology (Eichenfield et al., 2014). Plasma samples were collected from AD patients and healthy controls. We then performed fractionation and enrichment using an Oasis HLB solid-phase extraction column to obtain HLB-column-fractionated blood plasma (HFBP) according to previous established method (Ge et al., 2026; Wang et al., 2026). Here, HFBP^{AD} represents the fractionated plasma from atopic dermatitis patients, and HFBP^{H} denotes the fractionated plasma from healthy controls (Fig. 6a). This pretreatment removes high-molecular-weight plasma interferents and enriches low-abundance pruritogenic peptides, the key analytes targeted by our biosensor.

We next examined the electrical responses of the MRGPRX2–GFET itch receptor biosensor stimulated by HFBP^{AD} and HFBP^{H} (Fig. 6a). The electrical signal response was quantified on the basis of a Dirac point shift exceeding the baseline level observed in control experiments (1×HBSS). Compared with HFBP^{H}, which is derived from healthy individuals, HFBP^{AD} induced a stronger electrical response in the MRGPRX2–GFET itch receptor biosensor. Dose-dependent analysis revealed that increasing concentrations of the endogenous peptide fraction (from 0 ng/μL to 200 ng/μL) elicited a characteristic shift in V_{cnp}. The corresponding transfer curves shifted from 0.24 V to 0.18 V (Fig. 6b and Fig. S6a–g). The dose−response data revealed a characteristic sigmoidal increase in signal intensity. A saturable binding curve obtained through nonlinear fitting confirmed the high affinity of the sensor for the target protein (Fig. 6c). Notably, across multiple concentration gradients, the Dirac point voltage shift was greater in patient samples than in normal control samples, demonstrating a greater response in patient samples (Fig. 6d). To exclude nonspecific adsorption from complex plasma matrices, we tested bare GFET and PBASE-only control devices. These controls exhibited marginal Dirac point shifts ($\Delta V_{cnp} < 2$ mV, <8% of the full sensor response), indicating that the recorded signals are specifically attributable to MRGPRX2–target interactions rather than background matrix effects (Fig. S6h). To evaluate the real-world performance of the MRGPRX2-mediated GFET itch sensor, we further tested it using undiluted clinical plasma samples from AD patients and healthy individuals. The sensor response in plasma from patients with AD was significantly greater than that in plasma from healthy controls, indicating that the presence of endogenous pruritogens could be effectively translated into a quantifiable electrical signal and supporting its potential for clinical auxiliary diagnosis (Fig. 6e, Fig. S7a, Fig. S8a and Table S1). Receiver operating characteristic (ROC) curve analysis demonstrated excellent diagnostic performance, with an area under the curve (AUC) of 0.9669 for distinguishing AD patients from healthy individuals (Fig. 6f). The optimal cutoff value determined by ROC analysis was 24.63. Based on this threshold, confusion matrix analysis further confirmed a sensitivity of 93.75% and a specificity of 87.50%, validating the high accuracy and reliability of this sensing strategy for clinical sample testing (Fig. 6g).

Our findings indicated that the MRGPRX2–GFET itch receptor biosensor could respond to itch-related irritants in the blood, providing a novel tool not only for early risk assessment but also for potentially subclassifying AD endotypes. No itch irritant biosensors have been reported previously. In our concurrently submitted manuscript, we developed a cell-based activity measurement method, which enabled the detection of itch receptor activity and revealed close relationships between elevated MRGPRX1 activity and both MRGPRX2 activity and AD activity. In contrast to the cell assays used in our parallel research, the MRGPRX2–GFET itch receptor biosensor significantly reduced the assay preparation time (from 3 days to 2 min), was conveniently transferrable (it did not require a cell culture room or sterilized conditions) and was more sensitive. Therefore, the MRGPRX2–GFET itch receptor biosensor offered a transformative approach to complement previous

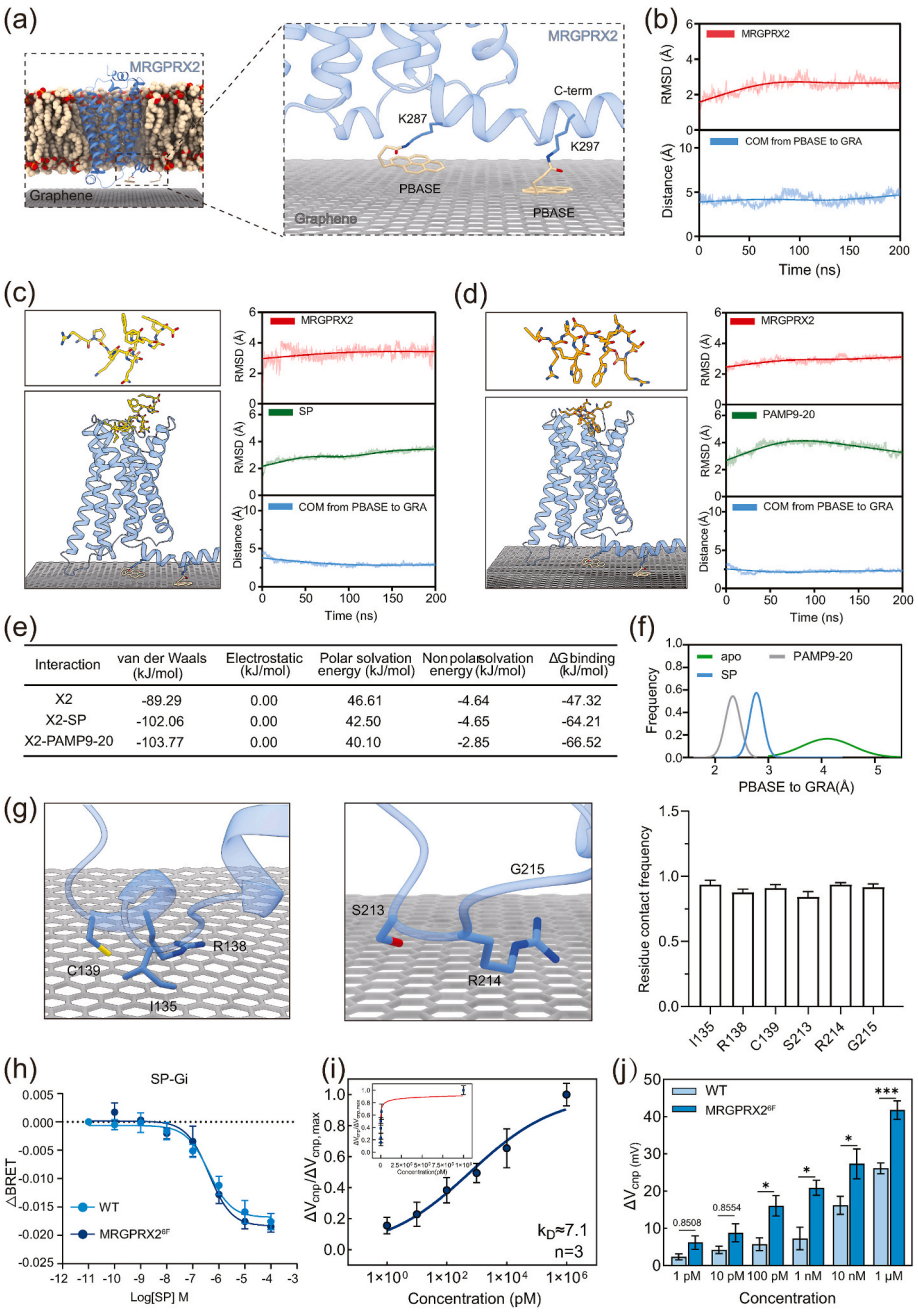

Interaction	van der Waals (kJ/mol)	Electrostatic (kJ/mol)	Polar solvation energy (kJ/mol)	Non polar solvation energy (kJ/mol)	ΔG binding (kJ/mol)
X2	-89.29	0.00	46.61	-4.64	-47.32
X2-SP	-102.06	0.00	42.50	-4.65	-64.21
X2-PAMP9-20	-103.77	0.00	40.10	-2.85	-66.52

Fig. 5. Molecular mechanism of electrical signal generation in GFET-Based itch-receptor biosensor.

(a) Binding mode of the MRGPRX2–PBASE–graphene complex. The receptor is covalently linked to the PBASE molecule via lysine residues at the intracellular surface, and the pyrene group of PBASE anchors onto the graphene sheet through π–π stacking interactions.

(b) Molecular dynamics simulation of the MRGPRX2–PBASE–graphene system without ligand binding. Upper panel: RMSD of MRGPRX2 during 200-ns simulation. Lower panel: center-of-mass distance between PBASE and graphene.

(c) MRGPRX2–ligand (SP) complex model (left) and molecular dynamics analysis showing RMSD of MRGPRX2 and SP ligand, and center-of-mass distance between PBASE and graphene (right).

(d) MRGPRX2–ligand (PAMP9-20) complex model (left) and molecular dynamics analysis showing RMSD of MRGPRX2 and PAMP9-20 ligand, and center-of-mass distance between PBASE and graphene (right).

(e) Binding free energy of the MRGPRX2–graphene interaction obtained from MM/GBSA calculations.

(f) Comparison of the center-of-mass distance between PBASE and graphene in apo and ligand-bound (SP and PAMP9-20) MRGPRX2 systems.

(g) Amino acid residues of MRGPRX2 (I135, R138, C139, S213, R214, G215) involved in graphene interaction and their contact frequencies in ligand-bound systems.

(h) Dose response curves of Gi dissociation in MRGPRX2 or MRGPRX2^{6F} (I135F, R138F, C139F, S213F, R214F, G215F) overexpressing HEK293 cells in response to stimulation with SP.

(i) Normalized Dirac point shift $\Delta V_{cnp}/\Delta V_{cnp,\ max}$ as a function of SP concentrations.

(j) Comparison of transfer characteristic curves of GFET-Based MRGPRX2 and MRGPRX2^{6F} biosensors measured upon exposure to different SP concentrations in PBS.

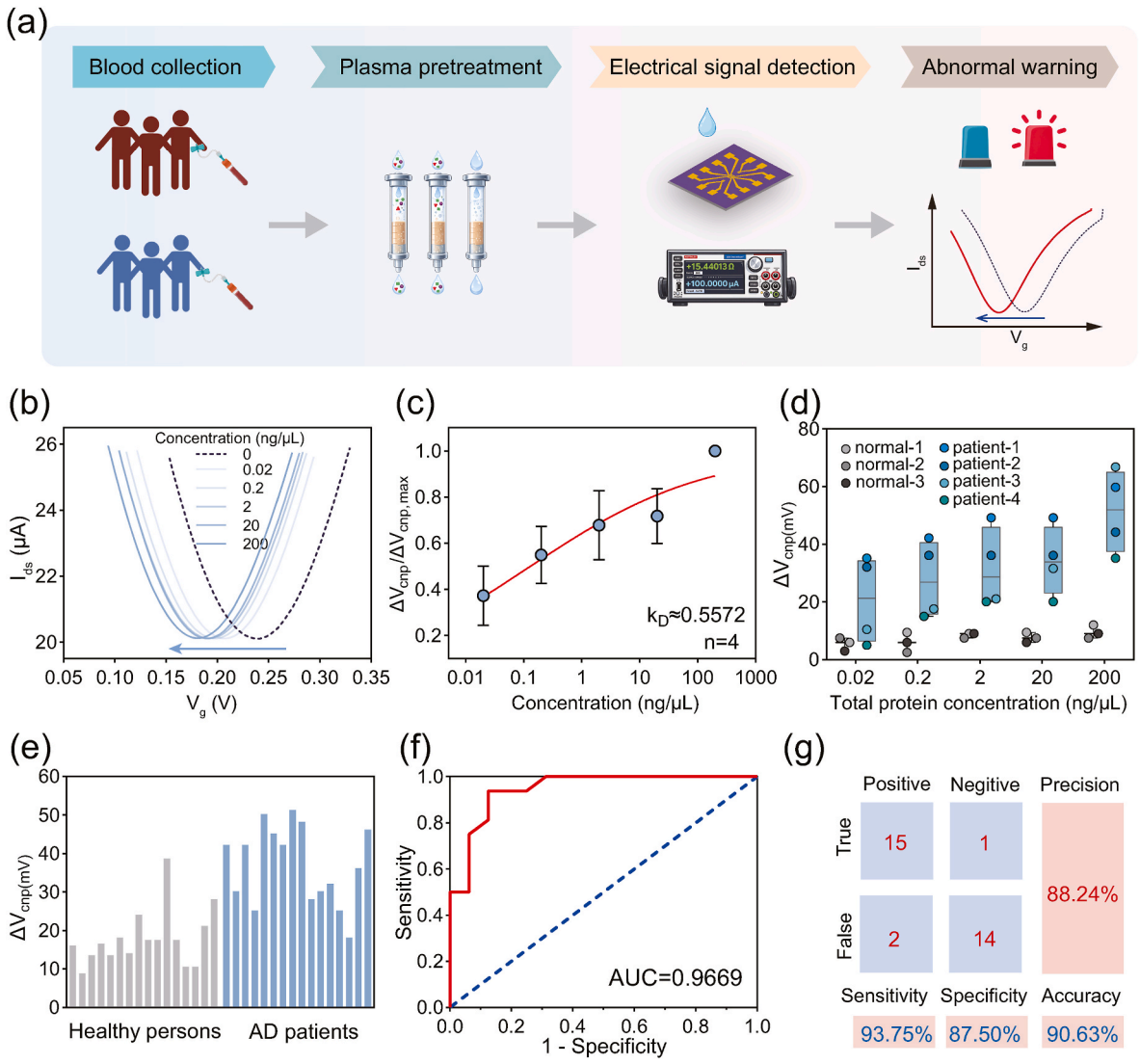

Fig. 6. Biomarker detection in clinical human blood samples.
(a) Schematic diagram of GFET detection of clinical blood samples.
(b-c) Transfer characteristic curves measured when the GFET-based itch-receptor biosensor was exposed to clinical samples ranging from 0 to 200 ng/μL from AD patients (b). Normalized Dirac point shift $\Delta V_{cnp}/\Delta V_{cnp,\ max}$ as a function of total protein concentration in HFBP (c).
(d) Sensing response of GFET-based itch-receptor biosensor to clinical samples from healthy individuals (gray) and AD patients (blue).
(e) Sensing response of GFET-based itch-receptor biosensor to clinical plasma samples from healthy individuals (gray) and AD patients (blue).
(f) Testing group ROC analysis curve based on different clinical plasma samples.
(g) Confusion matrix and prediction performance metrics derived from the optimal cutoff value of the ROC curve, including sensitivity, specificity, accuracy, and precision for clinical sample classification. (For interpretation of the references to colour in this figure legend, the reader is referred to the Web version of this article.)

diagnostic strategies and guide individualized therapeutic interventions.

3. Discussion

The development of biosensors that leverage the molecular machinery of biological sensory systems offers promising avenues for detecting physiological, pathological and environmental stimuli. These biosensors have broad applications in environmental monitoring, pathological diagnosis and timely warning to prevent damage from occurring. While receptors for vision, olfaction, and taste have been successfully incorporated into biosensing platforms, somatosensory modalities such as pruritus (itch) have not been explored. Chronic itch, a challenging symptom of conditions such as AD and ACD, is known to be mediated by a particular set of GPCRs. However, practical tools for the rapid detection of irritants that elicit itch in clinical biofluids or environmental habitats are lacking. In this study, we developed an initial bioelectronic sensor based on a human itch receptor integrated with a graphene GFET to address this need, and this MRGPRX2–GFET biosensor can convert ligand-binding events into measurable electrical signals, showing promising sensitivity and specificity and an initial ability to distinguish between plasma samples from AD patients and healthy controls.

Our study establishes a prototypical strategy for itch biosensor construction. We developed a protocol for the expression and purification of functional MRGPRX2 that could covalently immobilize the itch receptor onto graphene via PBASE, maintaining its ligand selectivity, binding potency and response efficacy. PBASE selectively conjugates to intracellular lysine residues, spatially segregated from the extracellular orthosteric binding pocket. Thus, the hydrophobic, hydrogen-bonded and electrostatic intermolecular interactions that mediate ligand recognition remain structurally unperturbed, without changing receptor ligand selectivity or downstream signaling kinetics. Notably, despite

electrical screening, normalized readouts, and replicate testing across ten independently fabricated sensors to mitigate batch-to-batch signal drift and noise, intrinsic device-to-device variability arising from fabrication tolerances and heterogeneous receptor immobilization remains a barrier to further advancement.

Characterization of the biointerface using techniques such as Raman spectroscopy, FE-SEM, EDS, and AFM suggested successful sensor fabrication. The sensor responded to known MRGPRX2 agonists, including SP and PAMP9-20, in a concentration-dependent manner, with a detection limit for SP at approximately 7 pM. The minimal response observed in control sensors without the receptor to ligands for unrelated receptors points to the receptor-dependent nature of the signal.

Beyond empirical validation, our study provides a mechanistic insight of signal transduction in a GPCR-coupled GFET biosensor. A longstanding gap in the field has been the lack of understanding of how agonist-induced conformational changes in a membrane protein are physically transmitted to the transducer surface. By integrating all-atom MD simulations with experimental validation, we demonstrated that ligand binding to MRGPRX2 induces specific cytoplasmic rearrangements that strengthen van der Waals and π–π interactions at the receptor–graphene interface via the PBASE linker. Engineering six cytoplasmic residues to phenylalanine ($MRGPRX2^{6F}$) could enhance hydrophobic coupling and significantly amplify the electrical response without altering ligand potency. Therefore, we not only provide important mechanistic guidance for receptor-based biosensor design but also offer a rational design route to improve the biosensor response through computational simulation and mutation design.

Moreover, a distinguishing feature of our biosensor is its ability to analyze complex clinical matrices such as plasma. By capturing a distinct electrical "itch-print" from AD patient samples, our device demonstrates that the sensor effectively reports the integrated activity of MRGPRX2-mediated pruritogenic signaling, rather than merely quantifying the absolute concentration of a single pre-defined biomarker (e.g., SP). This functional bioactivity readout is conceptually aligned with physiologically relevant disease pathology, as it reflects the net effect of multiple endogenous ligands present in the sample. Our pilot clinical cohort yields robust diagnostic performance (AUC = 0.9669, sensitivity 93.75%, specificity 87.50%), verifying its diagnostic potential. While full clinical validation requires expanded multi-center cohorts, this platform offers key advantages over ELISA and cell-based assays: ultrafast detection within minutes and simplified sample handling. The modular platform permits simple incorporation of distinct itch receptors, paving the way for multiplexed "itch-print" panels to stratify subtypes of chronic pruritic disorders and monitor itch-triggering environmental substances.

4. Conclusion

In summary, we developed the first itch biosensor for itch-related irritant detection. The sensing mechanism capitalizes on the high specificity of receptor–ligand recognition, which enables exceptional sensitivity with a detection limit for SP reaching to approximately 7 pM. Moreover, the MRGPRX2–GFET itch receptor biosensor achieves direct and rapid detection of clinical blood samples. Our computational MD simulation and mutational effects investigation offers mechanistic insights into the transduction of biological sensing to electrical signals within GFET-based biosensors and facilitates better GFET-based biosensor design and responses. Furthermore, our modular design lays the groundwork for incorporating other key itch receptors (e.g., MRGPRX1 and MRGPRX4), with the ultimate goal of creating a multiplexed "itch-print" sensor array capable of endotyping complex pruritic diseases or itch-related environmental changes.

5. Methods

5.1. Construct

The MRGPRX2 gene was cloned into pcDNA3.1 vector for functional assays and protein expression. The MRGPRX2 mutations were generated using the Quikchange mutagenesis kit (Stratagene). All of the constructs were verified by DNA sequencing.

5.2. Cell lines

Human embryonic kidney 293 (HEK293) cells were obtained from American Type Culture Collection (ATCC, Manassas, VA, USA) and cultured in DMEM with 10% fetal bovine serum and 1% penicillin/streptomycin at 37 °C with 5% CO_2. HEK293F cells were maintained in Cell wise-cw001 expression medium at 37 °C.

5.3. Expression and purification of the MRGPRX2

The MRGPRX2 was expressed in HEK293F cells. Cells were transfected with a plasmid-PEI mixture at 37 °C. After culture for 48 h, the cells were collected by centrifugation and cell pellets were stored at −80 °C for future use. Then cells expressed MRGPRX2 proteins were resuspended in 20 mM HEPES pH 7.4, 100 mM NaCl, 5 mM $CaCl_2$ and 3 mM $MgCl_2$ supplemented with complete Protease Inhibitor Cocktail tablets (Roche) by dounce homogenization. Then, solubilized by 0.5% (w/v) lauryl maltose neopentyl glycol (LMNG, Anatrace) supplemented with 0.05% (w/v) cholesteryl hemisuccinate (CHS) (Anatrace) for 2 h. Insoluble material was removed by centrifugation at 45,000 g for 45 min and the solubilized MRGPRX2 was purified using M1 anti-Flag affinity resin. The resin was washed with 20 column volumes of 20 mM HEPES pH 7.4, 100 mM NaCl, 3 mM $MgCl_2$, 5 mM $CaCl_2$, 50 μM C48/80, 0.01% (w/v) LMNG and 0.001% (w/v) CHS. The receptor was then eluted in buffer containing 20 mM HEPES pH 7.4, 100 mM NaCl, 0.01% (w/v) LMNG, 0.001% (w/v) CHS, 5 mM EGTA and 0.2 mg ml^{-1} Flag peptide. After concentration using an Amicon Ultra Centrifugal Filter (30 kDa molecular weight cut-off), the MRGPRX2 receptor was processed for size-exclusion chromatography on a Superdex 200 Increase 10/300 column (GE Healthcare).

5.4. The preparation of the GFET chip

The biosensor was fabricated following the authors' previous fabrication protocol (2020; Hao et al., 2024; Wang et al., 2019a; Zhang et al., 2025b). The photoresist was first spin-coated on the 285 nm SiO_2/Si wafer that was cleaned with acetone. Upon the process of exposure and developing, the electrodes (10 nm Cr/30 nm Au) were deposited on the wafer using the standard metal deposition techniques. Finally, the photoresist was released by dipping the chip in acetone with ultrasound for 5 min at room temperature. To transfer the graphene onto the biosensor, the device was first exposed to the oxygen plasma to clean the surface and increase the surface hydrophilicity. The synthesized graphene was then transferred onto the substrate using the wet floating-transfer method.

5.5. The functionalization strategy of GFET biosensors

To enhance the response of Field-Effect Transistors (FETs) for biosensing applications, functionalization of the graphene surface is employed to activate its sensing capabilities (2020; Hao et al., 2024; Wang et al., 2019a; Zhang et al., 2025b). 1-Pyrenebutanoic Acid Succinimidyl Ester (PBASE) is commonly used as a molecular anchor in graphene functionalization to facilitate the immobilization of biomolecules. A 10 mM PBASE solution was prepared using DMF as the solvent. The chip was then immersed in this solution for 4 h, followed by washing with pure DMF to remove unreacted reagent. After

functionalization, a solution of MRGPRX2 receptor was drop-cast onto the surface and incubated for 12–16 h overnight at 4 °C. Subsequently, the surface was washed with PBS buffer to remove unreacted proteins. A solution of 10 mM ethanolamine was then drop-cast to prevent nonspecific adsorption. Finally, the chip was rinsed with PBS buffer and soaked in PBS for biosensing detection. Target ligand solutions at various concentrations were introduced into the sensing area and conduct electrical signal detection.

5.6. Characterization

Microscope images were obtained with Leica Digital Microscope DVM6, SEM images were obtained with FEI Quanta 200FEG-SEM, and TEM images were obtained with JEOL JEM-1200EX. The Raman spectra were tested using Renishaw inVia micro-Raman, excitation laser wavelength 532 nm. The device's electrical properties and transfer curves were characterized by Keithley 2636 B sourcemeters.

5.7. Calculation of limit of detection (LOD)

As previously described, the sensing response was fitted using the Hill-Langmuir equation, a model widely applied in GFET biosensor studies to describe the relationship between normalized Dirac point shifts and target analyte concentrations (Wang et al. 2019b, 2021). Specifically, we first established calibration curves using the normalized Dirac point shifts corresponding to different target concentrations, followed by nonlinear fitting with the Hill-Langmuir equation. The relationship between the sensing response ΔV_{cnp} and the target ligand concentration C is expressed as:

$$\Delta V_{cnp} = \frac{\Delta V_{max} * C^n}{K_d^n + C^n}$$

where ΔV_{max} represents the maximum response signal, K_d represents the apparent dissociation constant, and n represents the Hill coefficient. The LOD was then calculated based on the 3σ criterion, where σ is the standard deviation of the blank sample signal. The response value corresponding to the blank signal plus 3σ was substituted into the inverse function of the Hill-Langmuir fitting equation to obtain the corresponding target concentration, which was defined as the LOD.

5.8. Patient recruitment

A total of 19 healthy controls and 20 participants with AD were recruited between December 2023 and February 2025 from the Department of Dermatology, Qilu Hospital of Shandong University A confirmed diagnosis of atopic dermatitis was determined by two dermatologists according to the criteria of Hanifin and Rajka (Hanifin and Rajka, 1980;Ständer, 2021) and the consensus criteria of the American Academy of Dermatology (Eichenfield et al., 2014). See Table S1 for patient details. Patients who were immunodeficient, pregnant, or had taken systemic corticosteroids/immunosuppressants 4 weeks before recruitment were excluded from the study. All healthy controls were enrolled with the following standardized criteria: no history of atopic dermatitis, chronic eczema, urticaria, allergic rhinitis, asthma or other allergic and pruritic skin/systemic diseases; no personal or immediate family history of hereditary skin diseases or severe autoimmune disorders; no use of glucocorticoids, immunosuppressants, antihistamines or other anti-pruritic/anti-inflammatory drugs within 4 weeks before sample collection; no acute infection, trauma or major surgical history within one month; non-pregnant and non-lactating female participants. The mean ages were 40.4 ± 4.5 years (AD) and 39.4 ± 3.3 years (controls), with no statistically significant difference (unpaired *t*-test, $p > 0.05$). Sex distribution was also balanced: AD group (10 male/10 female), control group (9 male/10 female), with no statistically significant difference (Fisher's exact test, $p > 0.05$). The study was approved by the Medical Ethics Committee of Qilu Hospital of Shandong University (KYLL-202311(YJ)-045). All participants provided written informed consent. Peripheral blood samples were centrifuged at 3000 rpm for 10 min at 4 °C to obtain plasma. The polypeptide protein components of AD patients and healthy individuals were enriched via Oasis PRiME HLB extraction cartridges according to the manufacturer's instructions.

5.9. Molecular dynamics simulations

MD simulations were carried out using GROMACS 2019.5 with the AMBER14SB force field for the MRGPRX2 receptor. The PBASE linker and graphene sheet were parameterized with the General AMBER Force Field (GAFF) to ensure consistency within the AMBER framework. All topology and coordinate files were prepared using CHARMM-GUI.

The MRGPRX2–PBASE–graphene complexes, including apo, SP-bound, and PAMP9-20-bound systems, were solvated in a periodic TIP3P water box with a size of approximately $90 \times 90 \times 120$ Å^3. A physiological ionic concentration of 0.15 M NaCl was added using the Monte Carlo ion placement method to neutralize the system charge. Each system was first subjected to 10,000 steps of energy minimization, with the first 5000 steps performed using the steepest descent method and the remaining 5000 using the conjugate gradient method. The minimized systems were gradually heated from 0 to 310 K in the NVT ensemble for 1 ns, followed by NPT equilibration for another 1 ns using a velocity-rescaling thermostat and Parrinello–Rahman barostat. Subsequently, 200-ns production simulations were performed under periodic boundary conditions at 310 K and 1 bar. Long-range electrostatics were calculated using the particle mesh Ewald (PME) method with a cutoff of 12 Å for nonbonded interactions. All covalent bonds involving hydrogen atoms were constrained using the LINCS algorithm, allowing a time step of 2 fs. Each simulation condition was repeated three times to ensure reproducibility.

5.10. Binding free energy calculation

The binding free energy between MRGPRX2 and the graphene surface was calculated using the gmx_MMPBSA package based on the molecular mechanics generalized Born surface area (MM/GBSA) method. The total binding free energy was decomposed into three major terms: (i) molecular mechanical potential energy in vacuum, (ii) polar solvation free energy, and (iii) non-polar solvation free energy. For each simulated system (apo, SP-bound, and PAMP9-20-bound), the last 50 ns of the 200-ns production trajectories were extracted for calculation, representing the equilibrated portion of the simulation. Default parameters of gmx_MMPBSA were employed, including the use of Bondi atomic radii, the generalized Born implicit solvent model, and a solvent probe radius of 0.14 nm for non-polar solvation energy estimation. All binding free energy results were averaged over three independent trajectories. The reported values represent theoretical estimates derived from force-field parameters and are used for comparative evaluation of MRGPRX2–graphene interaction strength under different ligand-binding conditions.

5.11. FlAsH BRET

As previously described, the S3 sensor, which labels the FlAsH motif at ECL2 of MRGPRX2 with Nluc inserted at the N-terminus, was adopted in the FlAsH-BRET assay (Yang et al., 2021a). In brief, purified S3 sensor of MRGPRX2-FlAsH proteins were labeled with 2.5 μM FlAsH-EDT_2 at 37 °C for 1 h. The proteins were suspended in BRET buffer (25 mM HEPES, 1 mM $CaCl_2$, 140 mM NaCl, 2.7 mM KCl, 0.9 mM $MgCl_2$, 0.37 mM NaH_2PO_4, 5.5 mM D-glucose, and 12 mM $NaHCO_3$, pH = 7) and transferred to black 96-well plates. After adding the luciferase substrate coelenterazine-h (working concentration, 5 μM), the agonist C48/80 (final concentration of 10^{-9}–10^{-3} M) and antagonists such as

paeonol (final concentration of 10^{-10}–10^{-4} M), BRET signals were measured via a Mithras LB940 microplate reader (Berthold Technologies), which was equipped with 440–480 nm excitation and 525–585 nm emission filters. The BRET signal was represented by calculating the ratio of the light emitted by FlAsH to the light emitted by Nanoluc.

5.12. The Gi dissociation assay

The Gi dissociation assay was performed as previously described (Yang et al., 2021a). Briefly, HEK293 cells were transiently co-transfected with Flag-MRGPRX2, Gi-Rluc8, Gβ3 and GFP2-Gγ9 and then cultured at 37 °C for 36–48 h. Cells were harvested by trypsinization, pelleted by centrifugation, and washed twice with BRET buffer (25 mM HEPES, 1 mM $CaCl_2$, 140 mM NaCl, 2.7 mM KCl, 0.9 mM $MgCl_2$, 0.37 mM NaH_2PO_4, 5.5 mM D-glucose, and 12 mM $NaHCO_3$, pH = 7). After resuspension in BRET buffer, cells were seeded into white 96-well plates at a density of 1×10^5 cells per well. Coelenterazine 400a (final concentration 5 μM) and test ligands were sequentially added, and BRET signals were measured using a Mithras LB940 microplate reader (Berthold Technologies) equipped with 400-nm excitation and 515-nm emission filters. The BRET ratio was calculated as the emission intensity at 515 nm divided by that at 400 nm. Ligand-induced changes are expressed as ΔBRET.

CRediT authorship contribution statement

Lulu Guo: Formal analysis, Resources, Supervision, Writing – original draft, Writing – review & editing. **Weifeng Zhang:** Data curation, Investigation, Methodology, Writing – original draft, Writing – review & editing. **Xuan Li:** Data curation, Investigation, Methodology, Validation, Visualization, Writing – original draft, Writing – review & editing. **Canyang Niu:** Software, Visualization, Writing – original draft. **Zili Liu:** Investigation, Methodology, Validation. **Zaiyu Zhang:** Investigation, Methodology, Software, Visualization. **Honghao Fan:** Visualization. **Xihe Gao:** Investigation, Methodology. **Kaiyu Wang:** Validation. **Haoran Liu:** Validation. **Chunhong Zhang:** Resources. **Ying Li:** Methodology, Resources. **Ziran Wang:** Data curation, Methodology, Resources. **Fan Yang:** Data curation, Resources, Supervision. **Guoqiang Li:** Investigation, Methodology, Validation, Writing – original draft, Writing – review & editing. **Jinpeng Sun:** Conceptualization, Funding acquisition, Resources, Supervision, Writing – original draft, Writing – review & editing.

Declaration of competing interest

The authors declare that they have no known competing financial interests or personal relationships that could have appeared to influence the work reported in this paper.

Acknowledgement

We thank Translational Medicine Sharing Platform of Advanced Medical Research Institute, Shandong University, for instrument availability. This work was supported by the Noncommunicable Chronic Diseases-National Science and Technology Major Project (2023ZD0507000 to L.-L. G.); National Science Fund for Distinguished Young Scholars grant (82425105 to J.-P. S.), the National Natural Science Foundation of China (82571288 to L.-L. G., 92353303 and 82421004 to F.Y., 52305606 to Z.-R. W. and 824B2018 to W.-F. Z.); the Shandong Provincial Taishan Scholars Program (tsqn202312342 to L.-L. G.); the National Key R&D Program of China (2023YFA1801100 and 2022YFC2702603 to F.Y., and 2023YFC2507801 to L.-L. G.); the Natural Science Foundation of Shandong Province (ZR202211230202 to F.Y. and ZR2023QE187 to Z.-R. W.); J.-P. S. is supported by the Tencent New Cornerstone Investigator Program.

Appendix A. Supplementary data

Supplementary data to this article can be found online at https://doi.org/10.1016/j.bios.2026.119064.

Data availability

No data was used for the research described in the article.

References

Afrooghe, A., Ahmadi, E., Babaei, M., Soltani, Z.E., Elahi, M., Shayan, M., Jafari, R.M., Dehpour, A.R., 2025. Lasmiditan ameliorates serotonergic itch in mice: possible involvement of 5-HT1F receptors. N-S Arch Pharmacol. 398 (2), 1535–1543.
Al Hamwi, G., Riedel, Y.K., Clemens, S., Namasivayam, V., Thimm, D., Muller, C.E., 2022. MAS-related G protein-coupled receptors X (MRGPRX): orphan GPCRs with potential as targets for future drugs. Pharmacol. Ther. 238, 108259.
Alemi, F., Kwon, E., Poole, D.P., Lieu, T., Lyo, V., Cattaruzza, F., Cevikbas, F., Steinhoff, M., Nassini, R., Materazzi, S., Guerrero-Alba, R., Valdez-Morales, E., Cottrell, G.S., Schoonjans, K., Geppetti, P., Vanner, S.J., Bunnett, N.W., Corvera, C. U., 2013. The TGR5 receptor mediates bile acid-induced itch and analgesia. J. Clin. Investig. 123 (4), 1513–1530.
Bader, M., Alenina, N., Andrade-Navarro, M.A., Santos, R.A., 2014. Mas and its related G protein-coupled receptors. Mrgprs. Pharmacol. Rev. 66 (4), 1080–1105.
Bains, G., Patel, A.B., Narayanaswami, V., 2011. Pyrene: a probe to study protein conformation and conformational changes. Molecules 16 (9), 7909–7935.
Baral, P., Mills, K., Pinho-Ribeiro, F.A., Chiu, I.M., 2016. Pain and itch: beneficial or harmful to antimicrobial defense? Cell Host Microbe 19 (6), 755–759.
Beaudry, F., Vachon, P., 2006. Determination of substance P in rat spinal cord by high-performance liquid chromatography electrospray quadrupole ion trap mass spectrometry. Biomed. Chromatogr. 20 (12), 1344–1350.
Bieber, T., 2022. Atopic dermatitis: an expanding therapeutic pipeline for a complex disease. Nat. Rev. Drug Discov. 21 (1), 21–40.
Bodily, T.A., Ramanathan, A., Wei, S.H., Karkisaval, A., Bhatt, N., Jerez, C., Haque, M.A., Ramil, A., Heda, P., Wang, Y., Kumar, S., Leite, M., Li, T., Zhao, J.L., Lal, R., 2023. In pursuit of degenerative brain disease diagnosis: dementia biomarkers detected by DNA aptamer- attached portable graphene biosensor. P Natl. Acad. Sci. USA 120 (47).
de Araujo, W.R., Lukas, H., Torres, M.D.T., Gao, W., de la Fuente-Nunez, C., 2024. Low-cost biosensor technologies for rapid detection of COVID-19 and future pandemics. ACS Nano 18 (3), 1757–1777.
Deng, F., Wan, J., Li, G., Dong, H., Xia, X., Wang, Y., Li, X., Zhuang, C., Zheng, Y., Liu, L., Yan, Y., Feng, J., Zhao, Y., Xie, H., Li, Y., 2024. Improved green and red GRAB sensors for monitoring spatiotemporal serotonin release in vivo. Nat. Methods 21 (4), 692–702.
Deng, L.W., Costa, F., Blake, K.J., Choi, S., Chandrabalan, A., Yousuf, M.S., Shiers, S., Dubreuil, D., Vega-Mendoza, D., Rolland, C., Deraison, C., Voisin, T., Bagood, M.D., Wesemann, L., Frey, A.M., Palumbo, J.S., Wainger, B.J., Gallo, R.L., Leyva-Castillo, J.M., Vergnolle, N., Price, T.J., Ramachandran, R., Horswill, A.R., Chiu, I. M., 2023. Drives itch and scratch-induced skin damage through a V8 protease-PAR1 axis. Cell 186 (24), 5375-+.
Eichenfield, L.F., Tom, W.L., Chamlin, S.L., Feldman, S.R., Hanifin, J.M., Simpson, E.L., Berger, T.G., Bergman, J.N., Cohen, D.E., Cooper, K.D., Cordoro, K.M., Davis, D.M., Krol, A., Margolis, D.J., Paller, A.S., Schwarzenberger, K., Silverman, R.A., Williams, H.C., Elmets, C.A., Block, J., Harrod, C.G., Smith Begolka, W., Sidbury, R., 2014. Guidelines of care for the management of atopic dermatitis: section 1. Diagnosis and assessment of atopic dermatitis. J. Am. Acad. Dermatol. 70 (2), 338–351.
Emrick, J.J., Mathur, A., Wei, J., Gracheva, E.O., Gronert, K., Rosenblum, M.D., Julius, D., 2018. Tissue-specific contributions of TMEM79 to atopic dermatitis and mast cell-mediated histaminergic itch. P Natl. Acad. Sci. USA 115 (51), E12091–E12100.
Flynn, C.D., Chang, D.R., Mahmud, A., Yousefi, H., Das, J., Riordan, K.T., Sargent, E.H., Kelley, S.O., 2023. Biomolecular sensors for advanced physiological monitoring. Nat. Rev. Bioeng. 1 (8), 560–575.
Ge, X.Y., Cheng, J., Zhang, L.J., Guo, L.L., Xiang, R., Lu, Y., Ning, S.L., Wang, K.Y., Zhu, K.K., Gao, M.X., Li, Y., Zhang, Y.S., Rong, N.K., Han, X., Zhang, M.H., Fang, L., Xu, Y.F., Zhao, S.W., Li, Q., Yang, F., Hao, Y., Chai, R.J., Yu, X., Yang, J.C., Sun, J.P., 2026. Identification of Or5v1/Olfr110 as an oxylipin receptor and anti-obesity target. Cell 189 (5).
Gin, A., Nguyen, P.D., Melzer, J.E., Li, C., Strzelinski, H., Liggett, S.B., Su, J., 2024. Label-free, real-time monitoring of membrane binding events at zeptomolar concentrations using frequency-locked optical microresonators. Nat. Commun. 15 (1).
Guo, L., Zhang, Y., Fang, G., Tie, L., Zhuang, Y., Xue, C., Liu, Q., Zhang, M., Zhu, K., You, C., Xu, P., Yuan, Q., Zhang, C., Liu, L., Rong, N., Peng, S., Liu, Y., Wang, C., Luo, X., Lv, Z., Kang, D., Yu, X., Zhang, C., Jiang, Y., Dong, X., Zhou, J., Liu, Z., Yang, F., Eric Xu, H., Sun, J.P., 2023. Ligand recognition and G protein coupling of the human itch receptor MRGPRX1. Nat. Commun. 14 (1), 5004.
Guttman-Yassky, E., Renert-Yuval, Y., Brunner, P.M., 2025. Atopic dermatitis. Lancet 405 (10478), 583–596.
Hanifin, J.M., Rajka, G., 1980. Diagnostic features of atopic dermatitis. Acta Derm. Venereol. 92, 44–47 (Stockh) Suppl.

Hao, Z., Fang, X., Wang, Z., Huang, C., Li, F., Luo, Y., Ying, Y., Ma, S., Jia, Y., Wang, X., Pan, Y., 2024. Intelligent wearable graphene nano-electronics with switchable surface wettability capabilities for autonomous sweat enrichment-purification-analysis (Adv. Funct. Mater. 41/2024). Adv. Funct. Mater. 34 (41), 2470237.
Jin, T., Li, S.Y., Zheng, H.L., Liu, X.D., Huang, Y., Ma, G., Zhao, Y.X., Zhao, X.T., Yang, L., Wang, Q.H., Wang, H.J., Gu, C.Y., Pan, Z.Q., Lin, F.Q., 2025. Gut microbes-spinal connection is required for itch sensation. Gut Microbes 17 (1).
Jogiraju, V., Pawar, P., Yager, J., Ling, J.H., Shen, G., Chiu, A., Hughes, E., Palaparthy, R., Carter, C., Singh, R., 2025. Pharmacokinetics and safety of once-yearly lenacapavir: a phase 1, open-label study. Lancet 405 (10485), 1147–1154.
Kharlamova, N., Dunn, N., Bedri, S.K., Jerling, S., Almgren, M., Faustini, F., Gunnarsson, I., Rönnelid, J., Pullerits, R., Gjertsson, I., Lundberg, K., Månberg, A., Pin, E., Nilsson, P., Hober, S., Fink, K., Fogdell-Hahn, A., 2021. False positive results in SARS-CoV-2 serological tests for samples from patients with chronic inflammatory diseases. Front. Immunol. 12.
Kühn, H., Kolkhir, P., Babina, M., Düll, M., Frischbutter, S., Fok, J.S., Jiao, Q.Q., Metz, M., Scheffel, J., Wolf, K., Kremer, A.E., Maurer, M., 2021. Mas-related G protein-coupled receptor X2 and its activators in dermatologic allergies. J. Allergy Clin. Immunol. 147 (2), 456–469.
Kim, K.H., Moon, D., An, J.E., Park, S.J., Seo, S.E., Ha, S., Kim, J., Kim, K., Phyo, S., Lee, J., Kim, H.Y., Kim, M., Park, T.H., Song, H.S., Kwon, O.S., 2022. Wireless portable bioelectronic nose device for multiplex monitoring toward food freshness/spoilage. Biosens. Bioelectron. 215.
Kumari, S.M.N.S., Suryabai, X.T., 2024. Sensing the future-frontiers in biosensors: exploring classifications, principles, and recent advances. ACS Omega 9 (50), 48918–48987.
Laliberte, K.E., Scott, P., Khan, N.I., Mahmud, M.S., Song, E.D., 2022. A wearable graphene transistor-based biosensor for monitoring IL-6 biomarker. Microelectron. Eng. 262.
Li, Z.M., Goebel, S., Reimann, A., Ungerer, M., 2020. Histo-ELISA technique for quantification and localization of tissue components. Sci Rep-Uk 10 (1).
Lieu, T., Jayaweera, G., Zhao, P.S., Poole, D.P., Jensen, D., Grace, M., McIntyre, P., Bron, R., Wilson, Y.M., Krappitz, M., Haerteis, S., Korbmacher, C., Steinhoff, M.S., Nassini, R., Materazzi, S., Geppetti, P., Corvera, C.U., Bunnett, N.W., 2014. The bile acid receptor TGR5 activates the TRPA1 channel to induce itch in mice. Gastroenterology 147 (6), 1417–1428.
Lin, H., Ma, C., Cai, K., Guo, L., Wang, X., Lv, L., Zhang, C., Lin, J., Zhang, D., Ye, C., Wang, T., Huang, S., Han, J., Zhang, Z., Gao, J., Zhang, M., Pu, Z., Li, F., Guo, Y., Zhou, X., Qin, C., Yi, F., Yu, X., Kong, W., Jiang, C., Sun, J.P., 2025. Metabolic signaling of ceramides through the FPR2 receptor inhibits adipocyte thermogenesis. Science 388 (6746) eado4188.
Liu, A.W., Zhang, Y.R., Chen, C.S., Edwards, T.N., Ozyaman, S., Ramcke, T., McKendrick, L.M., Weiss, E.S., Gillis, J.E., Laughlin, C.R., Randhawa, S.K., Phelps, C. M., Kurihara, K., Kang, H.M., Nguyen, S.N., Kim, J., Sheahan, T.D., Ross, S.E., Meisel, M., Sumpter, T.L., Kaplan, D.H., 2025. Scratching promotes allergic inflammation and host defense via neurogenic mast cell activation. Science 387 (6733) eadn9390.
Liu, B.Y., Chen, R.X., Wang, J., Li, Y.Y., Yin, C.Y., Tai, Y., Nie, H.M., Zeng, D.Y., Fang, J. F., Du, J.Y., Liang, Y., Shao, X.M., Fang, J.Q., Liu, B.Y., 2022. Exploring neuronal mechanisms involved in the scratching behavior of a mouse model of allergic contact dermatitis by transcriptomics. Cell. Mol. Biol. Lett. 27 (1).
Liu, X.Y., Liu, Z.C., Sun, Y.G., Ross, M., Kim, S., Tsai, F.F., Li, Q.F., Jeffry, J., Kim, J.Y., Loh, H.H., Chen, Z.F., 2011. Unidirectional cross-activation of GRPR by MOR1D uncouples itch and analgesia induced by opioids. Cell 147 (2), 447–458.
Liu, Y.F., Cao, C., Huang, X.P., Gumpper, R.H., Rachman, M.M., Shih, S.L., Krumm, B.E., Zhang, S.C., Shoichet, B.K., Fay, J.F., Roth, B.L., 2023. Ligand recognition and allosteric modulation of the human MRGPRX1 receptor. Nat. Chem. Biol. 19 (4), 416-+.
Meixiong, J., Anderson, M., Limjunyawong, N., Sabbagh, M.F., Hu, E., Mack, M.R., Oetjen, L.K., Wang, F., Kim, B.S., Dong, X., 2019. Activation of mast-cell-expressed mas-related G-Protein-Coupled receptors drives non-histaminergic itch. Immunity 50 (5), 1163–1171 e1165.
Meixiong, J., Dong, X.Z., 2017. Mas-related G protein-coupled receptors and the biology of itch sensation. Annu. Rev. Genet. 51, 103–121.
Michaels, L.A., Ohene-Frempong, K., Zhao, H., Douglas, S.D., 1998. Serum levels of substance P are elevated in patients with sickle cell disease and increase further during vaso-occlusive crisis. Blood 92 (9), 3148–3151.
Nyberg, F., Legreves, P., Terenius, L., 1985. Identification of Substance-P precursor forms in human-brain tissue. P Natl. Acad. Sci. USA 82 (11), 3921–3924.
Ohno, Y., Maehashi, K., Matsumoto, K., 2010. Label-free biosensors based on aptamer-modified graphene field-effect transistors. J. Am. Chem. Soc. 132 (51), 18012–18013.
Ohsawa, Y., Hirasawa, N., 2012. The antagonism of histamine H1 and H4 receptors ameliorates chronic allergic dermatitis via anti-pruritic and anti-inflammatory effects in NC/Nga mice. Allergy 67 (8), 1014–1022.
Park, S.C., Jeong, H.J., Heo, M., Shin, J.H., Ahn, J.H., 2021. Carbon nanotube-based ion-sensitive field-effect transistors with an On-Chip reference electrode toward wearable sodium sensing. Acs Appl. Electr. Ma 3 (6), 2580–2588.
Prevalence and attributable health burden of chronic respiratory diseases, 1990-2017: a systematic analysis for the global burden of disease study 2017. Lancet Respir. Med. 8 (6), 2020, 585–596.
Qing, R., Xue, M.T., Zhao, J.Y., Wu, L.D., Breitwieser, A., Smorodina, E., Schubert, T., Azzellino, G., Jin, D., Kong, J., Palacios, T., Sleytr, U.B., Zhang, S.G., 2023. Scalable biomimetic sensing system with membrane receptor dual-monolayer probe and graphene transistor arrays. Sci. Adv. 9 (29).
Ren, H.H., Liang, K., Li, D.W., Chen, Y.T., Tang, Y.J., Wang, Y., Li, F.F., Liu, G.L., Zhu, B. W., 2023. Field-effect transistor-based biosensor for pH sensing and mapping. Adv. Sensor Res. 2 (8).
Rezaei, B., Khayamian, T., Majidi, N., Rahmani, H., 2009. Immobilization of specific monoclonal antibody on Au nanoparticles for hGH detection by electrochemical impedance spectroscopy. Biosens. Bioelectron. 25 (2), 395–399.
Roy, S., Chompunud Na Ayudhya, C., Thapaliya, M., Deepak, V., Ali, H., 2021. Multifaceted MRGPRX2: new insight into the role of mast cells in health and disease. J. Allergy Clin. Immunol. 148 (2), 293–308.
Seo, S.E., Cho, S., Kim, K.H., Lee, S., Lee, J., Cha, Y.K., Ryu, Y.S., Park, T.H., Song, H.S., Kwon, O.S., 2025. Nondestructive methodology with discerning fruit freshness biomarker compounds using olfactory receptor nanodisc-loaded graphene transistors. Biosens. Bioelectron. 281.
Son, M., Lee, J.Y., Ko, H.J., Park, T.H., 2017. Bioelectronic nose: an emerging tool for odor standardization. Trends Biotechnol. 35 (4), 301–307.
Son, M., Park, T.H., 2018. The bioelectronic nose and tongue using olfactory and taste receptors: analytical tools for food quality and safety assessment. Biotechnol. Adv. 36 (2), 371–379.
Ständer, S., 2021. Atopic dermatitis. N. Engl. J. Med. 384 (12), 1136–1143.
Su, J.Y., Li, Y.R., Xie, D.D., Jiang, J., 2023. Vertical 0.6 V sub-10 nm oxide-homojunction transistor gated by a silk fibroin/sodium alginate crosslinking hydrogel for pain-sensitization enhancement emulation. Mater. Horiz. 10 (5), 1745–1756.
Voisin, T., Chiu, I.M., 2019. Mast cells get on your nerves in itch. Immunity 50 (5), 1117–1119.
Wang, J.L., Sha, X.Y., Shao, Y., Zhang, Z.H., Huang, S.M., Lin, H., Gan, S.Y., Zhang, N., Xia, X.Y., Sun, Y.N., Ding, J.H., Zhao, R.Q., Cheng, J., Shang, P., Wang, J.P., Liu, Y.J., Yang, F., Xiao, P., Wang, L.W., Zhao, D.Y., Tang, Y., Tie, L., Du, Y., Zhang, Y., He, J. F., Sun, J.P., 2026. Elucidating pathway-selective biased CCKBR agonism for alzheimer's disease treatment. Cell 189 (2).
Wang, Z., Hao, Z., Yu, S., De Moraes, C.G., Suh, L.H., Zhao, X., Lin, Q., 2019a. An ultraflexible and stretchable aptameric graphene nanosensor for biomarker detection and monitoring. Adv. Funct. Mater. 29 (44).
Wang, Z.R., Hao, Z., Wang, X.J., Huang, C., Lin, Q., Zhao, X.Z., Pan, Y.L., 2021. A flexible and regenerative aptameric graphene-nafion biosensor for cytokine storm biomarker monitoring in undiluted biofluids toward wearable applications. Adv. Funct. Mater. 31 (4).
Wang, Z.R., Hao, Z., Yu, S.F., De Moraes, C.G., Suh, L.H., Zhao, X.Z., Lin, Q., 2019b. An ultraflexible and stretchable aptameric graphene nanosensor for biomarker detection and monitoring. Adv. Funct. Mater. 29 (44).
Wang, Z.R., Hao, Z., Yu, S.F., Huang, C., Pan, Y.L., Zhao, X.Z., 2020. A wearable and deformable graphene-based affinity nanosensor for monitoring of cytokines in biofluids. Nanomaterials-Basel 10 (8).
Yang, F., Guo, L., Li, Y., Wang, G., Wang, J., Zhang, C., Fang, G.X., Chen, X., Liu, L., Yan, X., Liu, Q., Qu, C., Xu, Y., Xiao, P., Zhu, Z., Li, Z., Zhou, J., Yu, X., Gao, N., Sun, J.P., 2021a. Structure, function and pharmacology of human itch receptor complexes. Nature 600 (7887), 164–169.
Yang, J., Li, G.X., Wang, W.X., Shi, J.L., Li, M., Xi, N., Zhang, M.J., Liu, L.Q., 2021b. A bio-syncretic phototransistor based on optogenetically engineered living cells. Biosens. Bioelectron. 178.
Yang, J., Zhao, T.J., Fan, J.P., Zou, H.B., Lan, G.Y., Guo, F.S., Shi, Y.C., Ke, H., Yu, H.S., Yue, Z.W., Wang, X., Bai, Y.J., Li, S., Liu, Y.J., Wang, X.M., Chen, Y., Li, Y.L., Lei, X. G., 2024. Structure-guided discovery of bile acid derivatives for treating liver diseases without causing itch. Cell 187 (25).
Yang, Z., Ping, Y.Q., Wang, M.W., Zhang, C., Zhou, S.H., Xi, Y.T., Zhu, K.K., Ding, W., Zhang, Q.Y., Song, Z.C., Zhao, R.J., He, Z.L., Wang, M.X., Qi, L., Ullmann, C., Ricken, A., Schöneberg, T., Gan, Z.J., Yu, X., Xiao, P., Yi, F., Liebscher, I., Sun, J.P., 2025. Identification, structure, and agonist design of an androgen membrane receptor. Cell 188 (6), 1589–1604.e1524.
Zhang, J., Luo, B., Fan, Z., Ma, X., Pu, Y., Liu, X., 2025a. Liquid chromatography-tandem mass spectrometry-based recalibration reduces inter-platform variability in aldosterone detection across chemiluminescence immunoassay platforms. Clin. Chim. Acta, 120604.
Zhang, Z., Zhang, L., Huang, Y., Wang, Z., Ren, Z., 2025b. A planar-gate graphene field-effect transistor integrated portable platform for rapid detection of Colon cancer-derived exosomes. Biosensors 15 (4), 207.
Zheng, Y., Cai, R., Wang, K., Zhang, J., Zhuo, Y., Dong, H., Zhang, Y., Wang, Y., Deng, F., Ji, E., Cui, Y., Fang, S., Zhang, X., Zhang, K., Wang, J., Li, G., Miao, X., Wang, Z., Yang, Y., Li, S., Grimm, J., Johnsson, K., Schreiter, E., Lavis, L., Chen, Z., Mu, Y., Li, Y., 2024. In vivo multiplex imaging of dynamic neurochemical networks with designed far-red dopamine sensors. bioRxiv.